Novel technologies for mitigation of cone-beam artifacts in C-arm CT imaging of the head

Zijia Guo, Günter Lauritsch, Andreas Maier, Frédéric Noo

***Abstract*—Cone-beam (CB) computed tomography (CT) using a floor- or ceiling-mounted C-arm system or using a robotic C-arm system has become a valuable tool in interventional radiology. This technology is typically used with a circular short-scan (SS) data acquisition geometry. As it is well-known, this geometry does not provide complete data for exact reconstruction. Furthermore, the classical SS-FDK algorithm, which is often employed, exacerbates CB artifacts by applying data redundancy weights that are not exact. In this paper, we are interested in mitigating CB artifacts in C-arm CT imaging of the head. We suggest a rebinning algorithm that allows transforming data from such systems into data acquired in an ideal geometry. This rebinning algorithm enables utilization of advanced CB reconstruction methods to mitigate CB artifacts. We extensively evaluated the performance of the rebinning algorithm using the FORBILD head phantom as well as a cylindrical phantom to assess MTF and SSP. The results show strong performance of the rebinning algorithm for geometry deviations encountered in practice. Furthermore, we have applied the rebinning algorithm to real data of an anthropomorphic phantom. This additional experiment demonstrated clinical value of our rebinning algorithm, particularly as a strong mitigation of CB artifacts can be seen in comparison with the SS-FDK algorithm. Last, we showed that data acquisition with the equivalent of a gantry tilt may provide, in terms of CB artifacts, additional improvements within the brain region.**

I. Introduction

Cone-beam (CB) computed tomography (CT) using a floor- or ceiling-mounted C-arm system or using a robotic C-arm system has become a valuable tool in interventional radiology. Often, this technology is referred to as C-arm CT imaging. Its value primarily lies in its ability to provide the interventional radiologist with immediate feedback during a procedure, so that lengthy transfers to a CT scanner room can be avoided, which reduces both risks to the patient and financial costs. Over time, there has been a continuous clinical request for improvements in C-arm CT image quality, to improve clinical outcomes as well as to facilitate the development of novel minimally-invasive procedures.

The circular short-scan (SS) data acquisition geometry is typically used in C-arm CT. As it is well-known, this geometry does not provide complete data for exact reconstruction. Furthermore, the classical SS-FDK algorithm, which is often employed, exacerbates CB artifacts by applying data redundancy weights that are not exact. In this paper, we are interested in mitigating CB artifacts in C-arm CT imaging of the head. Due to the complex structure of the human skull, CB artifacts can sometimes be very pronounced. Unusual skull appearance, due to fractures or intentional temporary skull bone removal, can make the problem worse.

F. Noo and Z. Guo are with the Department of Radiology, University of Utah, Salt Lake City, Utah, USA. G. Lauritsch is with Siemens Healthcare, GmbH. A. Maier is with the University of Erlangen-Nürnberg, Germany, and so is Z. Guo as well.

There are analytical methods that produce better results than the SS-FDK algorithm, by properly weighting the data. A first such method was suggested in [1], where smooth weights were employed in a filtered-backprojection framework. Later, [2] suggested a variant of this method, called the ACE algorithm, that uses discontinuous weigths. The ACE method offers the advantage of a more efficient filtering step and better use of photon statistics, but these advantage comes at the cost of higher sensitivity to slight anatomical variations during scanning, which could occur due to involuntary patient motion or injection of a contrast agent. Other examples of analytical or semi-analytical methods include [3], [4]. Analytical methods are not straightforward to use in C-arm CT because they are developed for ideal data acquisition geometries whereas the CB projections in C-arm CT present non-negligible geometrical deviations from this ideal setting. In this work, we suggest a data rebinning algorithm that allows overcoming this issue. The performance of this algorithm will be demonstrated using both computer-simulated and real data.

An additional way to mitigate CB artifacts in C-arm CT imaging of the head may be the application of a tilt to the scanning geometry, similar to the gantry-tilt used in diagnostic CT. The gantry tilt in CT is known to be highly preferred by neuroradiologists because it results in images of higher quality. To our knowledge, the idea of using a similar tilt in C-arm CT imaging of the head has never been explored. We will report as well early results in this direction, using real data of an anthropomorphic head phantom.

II. Background

In this section, we review the ideal geometry and briefly discuss deviations from this geometry that are observed in real measurements.

A. Ideal geometry

Ideally, the source positions in C-arm CT imaging using a short-scan acquisition would lie on a circular arc. Ideally, the detector at each position would also be oriented so as to be parallel to both the tangent to the source trajectory at the local source position and the axis orthogonal to the plane of the circular arc. Moreover, the orthogonal projection of the source onto the detector plane would remain fixed during the scan.

Mathematically, we describe the ideal geometry as follows. Given a 3-D Cartesian system of coordinates, x, y and z, the circular arc is centered on the origin, O, in the plane $z = 0$.

The source position on this arc is then described by a polar angle λ:

$$\vec{a}(\lambda) = (R\cos\lambda, R\sin\lambda, 0)^{\mathrm{T}} \tag{1}$$

where R is the radius of the arc and $\lambda \in [-\gamma_m, \pi+\gamma_m]$. Angle $\gamma_m \in (0, \pi/2)$ defines the radius, $R\sin\gamma_m$, of a cylindrical region-of-interest (ROI) centered on the origin and parallel to the z-axis. When the source position is at $\vec{a}(\lambda)$, the detector plane is spanned by vectors

$$\vec{e}_u(\lambda) = (-\sin\lambda, \cos\lambda, 0)^{\mathrm{T}} \tag{2}$$

$$\vec{e}_v(\lambda) = (0, 0, 1)^{\mathrm{T}} \tag{3}$$

Thus, vector

$$\vec{e}_w(\lambda) = \vec{e}_u(\lambda) \times \vec{e}_v(\lambda) = (\cos\lambda, \sin\lambda, 0)^{\mathrm{T}} \tag{4}$$

points towards the source. The distance between the source and the detector plane is a fixed constant D in this direction.

Detector pixels are identified by Cartesian coordinates (u, v) in the detector plane, with u and v measured along $\vec{e}_u$ and $\vec{e}_v$, respectively. The origin $(u, v) = (0, 0)$ corresponds to the orthogonal projection of the source onto the detector. The direction of an X-ray beam that starts at $\vec{a}(\lambda)$, that goes through a point Q within the ROI, and that hits the detector plane at (u, v) is given by a unit vector $\vec{\alpha}$ that can be expressed as:

$$\vec{\alpha}(\lambda, u, v) = \frac{u\vec{e}_u + v\vec{e}_v - D\vec{e}_w}{\sqrt{u^2 + v^2 + D^2}} \tag{5}$$

and

$$\vec{\alpha}(Q, \vec{a}(\lambda)) = \frac{\vec{OQ} - \vec{a}(\lambda)}{||\vec{OQ} - \vec{a}(\lambda)||} \tag{6}$$

B. Non-ideal geometry

Due to various mechanical forces, the CB projections acquired in C-arm CT are known to only approximate the desired ideal configuration. As illustrated in Figure 1, deviations are observed in the source position, as well as in the position and orientation of the detector. Fortunately, for many C-arms used in interventional radiology, the deviations are reproducible. Hence, geometrically-accurate reconstruction can be achieved using an off-line calibration process that identifies the source-detector position for each projection. Using homogeneous coordinates, the outcome of the calibration process can be summarized by 3×4 projection matrices.

III. Rebinning Process

In this section, we present the rebinning algorithm we suggest to transform the real data into CB measurements in an ideal geometry, using interpolation.

A. Trajectory Registration

The registration process is a rigid transformation from the world coordinate system to the ideal geometry. We start with a decomposition of each projection matrix into its components, which provides us with a vectorial description of the source and detector position in a world coordinate system attached to the calibration phantom. See e.g. [5] for a description of

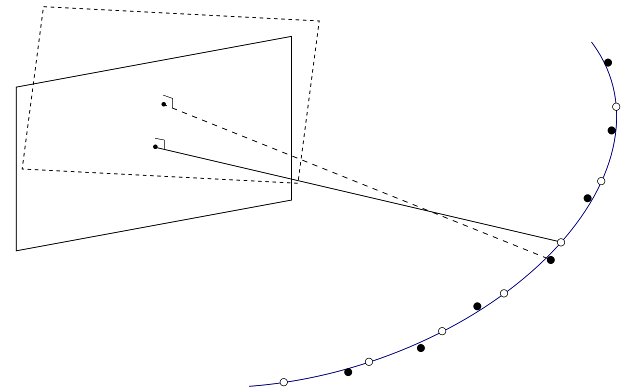

Fig. 1: Illustration of misalignment of the source and detector. The real and ideal source positions are indicated by a small black disk and a small open circle, respectively. The ideal detector placement is shown with solid lines, whereas the real detector placement, involving rotations and translations is shown with dashed lines. The line that connects the source position to its orthogonal projection onto the detector is shown in each case, using the same notation (solid/dashed line for ideal/real positions.)

this decomposition process. At this stage, the non-ideal source positions are known and we look for a plane that best fit these source positions. Let $\vec{q}_{i,j}$ represent a vector pointing from one real source position, $\vec{b}_i$, to another, $\vec{b}_j$. Thus,

$$\vec{q}_{i,j} = \vec{b}_j - \vec{b}_i \quad (i, j = 1, 2, 3, ...; i \neq j) \tag{7}$$

The normal to the sought plane, $\vec{e}_3$, is obtained by requiring it to be as perpendicular as possible to all vectors $\vec{q}_{i,j}$. I.e.,

$$\vec{e}_3 = \mathrm{argmin}_{\{\vec{e}_3\}} \left\{ \sum_{i,j} (\vec{q}_{i,j} \cdot \vec{e}_3)^2 - \beta\,(\vec{e}_3 \cdot \vec{e}_3 - 1) \right\} \tag{8}$$

where β is a Lagrange multiplier used to enforce unit length for $\vec{e}_3$. From here, we can obtain three unit orthogonal vectors, $\vec{e}_1$, $\vec{e}_2$ and $\vec{e}_3$, in the world coordinate system. We chose $\vec{e}_1 = \vec{b}_1/||\vec{b}_1||$ and $\vec{e}_2 = \vec{e}_3 \times \vec{e}_1$.

Next, we look for a point $\vec{x}_0 = (x_0, y_0, z_0)^T$ that is meant to be the center of the circular arc that best fits the source positions in a plane orthogonal to $\vec{e}_3$. Coordinate z_0 is obtained as the mean of the following dot products: $\vec{b}_i \cdot \vec{e}_3$. For x_0 and y_0, we apply fitting to the equation $(x-x_0)^2+(y-y_0)^2 = \hat{R}^2$. Using (x_i, y_i, z_i) for the coordinates of $\vec{b}_i$ along $\vec{e}_1$, $\vec{e}_2$ and $\vec{e}_3$, the fitting can be done through solution of a linear system of equations:

$$\begin{pmatrix} 2x_1 & 2y_1 & 1 \\ 2x_2 & 2y_2 & 1 \\ & ... & \\ 2x_i & 2y_i & 1 \\ & ... & \end{pmatrix} \begin{pmatrix} x_0 \\ y_0 \\ \hat{R}^2 - x_0^2 - y_0^2 \end{pmatrix} = \begin{pmatrix} x_1^2 + y_1^2 \\ x_2^2 + y_2^2 \\ ... \\ x_i^2 + y_i^2 \\ ... \end{pmatrix} \tag{9}$$

This system indirectly yields the center of the fitted circle, (x_0, y_0, z_0) as well as it radius, $\hat{R}$.

At this stage, we can rigidly transform the data geometry from the world coordinate system to the ideal geometry using both rotation and translation. Letting $Q = [\vec{e}_1, \vec{e}_2, \vec{e}_3]$, we evaluate

$$\vec{d}_i = Q^{\mathrm{T}}(\vec{b}_i - \vec{x}_0)\,, \tag{10}$$

which represents transformed source positions as aligned as possible with the ideal geometry, except for a rotation angle ϕ in the (x, y) plane. Angle ϕ is found as $\phi = -\gamma_m - \phi_1$ where ϕ_1 is the polar angle for $\vec{d}_1$.

Let

$$\Phi = \begin{pmatrix} \cos\phi & \sin\phi & 0 \\ -\sin\phi & \cos\phi & 0 \\ 0 & 0 & 1 \end{pmatrix} \quad (11)$$

Then, the following equation expresses the real source positions in the coordinate system of the ideal geometry

$$\vec{c}_i = \Phi^{\mathrm{T}} Q^{\mathrm{T}} (\vec{b}_i - \vec{x}_0) \quad (12)$$

Similar rotations are applied to find the vectors that orient the detector.

B. Data rebinning

After registration, the measurements are unchanged, but we have an expression for the source and detector positions that are close to the ideal geometry. The data rebinning process amounts to obtaining projection values at ideal source positions, $\vec{a}(\lambda)$, from the projection data at source positions $\vec{c}_i$ using linear interpolation. The ideal-geometry data are created at $\lambda = -\gamma_m + k\Delta\lambda$, $k = 0, 1, 2, \ldots$. The increment $\Delta\lambda$ is obtained as $\Delta\lambda = (\pi + 2\gamma_m)/(N-1)$, where N is the number of projections and $\pi + 2\gamma_m$ is the polar angle difference between $\vec{c}_1$ and $\vec{c}_N$.

We now explain how the data is created at $\vec{a}(\lambda_k)$. The X-ray beam that starts at $\vec{a}(\lambda_k)$ and hits the detector plane at (u, v) with direction $\vec{\alpha}(\lambda_k, u, v)$ is identified with a line $\mathcal{L}$. Let M be a point on $\mathcal{L}$ that is more or less centered within the scanned ROI. Let $\vec{c}_j$ and $\vec{c}_{j+1}$ be the two registered source positions that are closest to $\vec{a}(\lambda_k)$, with $\psi_j < \lambda_k < \psi_{j+1}$ if ψ_j is the polar angle for $\vec{c}_j$. The X-ray beam that comes from $\vec{c}_j$ (resp. $\vec{c}_{j+1}$) and passes through M has direction $\vec{\alpha}(M, \vec{c}_j)$ (resp. $\vec{\alpha}(M, \vec{c}_{j+1})$). See the illustration in Figure 2. The projection value at (u, v) for $\vec{a}(\lambda_k)$ is interpolated from the projection data for $\vec{c}_j$ at (u_j^*, v_j^*) and the projection data for $\vec{c}_{j+1}$ at (u_{j+1}^*, v_{j+1}^*). The coordinates (u_j^*, v_j^*) are found from the detector positioning vectors to match the line of direction $\vec{\alpha}(M, \vec{c}_j)$ through $\vec{c}_j$. The same is done for (u_{j+1}^*, v_{j+1}^*).

Because the data rebinning step requires interpolation in (u, v), as well as in the polar angle, some resolution loss may be expected. To compensate for the anticipated resolution loss in (u, v), we pre-filter the original data using a frequency-boosting filter that amounts to a product of sinc^2 functions in the frequencies corresponding to u and v. The interpolation in the direction of the polar angle is shift-variant and may not be as easily compensated for. However, we anticipate that no compensation should be needed because this interpolation occurs in the direction of the backprojection.

IV. Evaluations

In this section, we present evaluation results of our method using both computer-simulated data of the FORBILD head phantom and real data of an anthropomorphic head phantom.

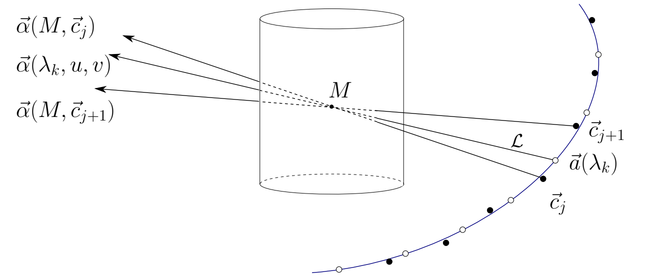

Fig. 2: Illustration of data rebinning process. The curve represents the ideal trajectory with source samples (white dots) on it. The registered real source positions (solid black dots) are close to the ideal trajectory. X-ray beam $\mathcal{L}$ corresponds to a desired line integral at $\vec{a}(\lambda_k)$ and M is a central point on $\mathcal{L}$. The two closest registered source positions that surround $\vec{a}(\lambda_k)$ are $\vec{c}_j$ and $\vec{c}_{j+1}$. The desired line integral is interpolated (in polar angle) from two oblique line integrals through M, one of which starts at $\vec{c}_j$ with direction $\vec{\alpha}(M, \vec{c}_j)$ and the other one at $\vec{c}_{j+1}$ with direction $\vec{\alpha}(M, \vec{c}_{j+1})$.

A. Experiment set up

Both ideal and non-ideal geometries were used to generate CB data of the FORBILD head phantom. The non-ideal geometry was based on projection matrices that characterize the non-ideal geometry of a real data acquisition on a research-dedicated Siemens Artis C-arm system. The parameters for the ideal geometry where obtained through the above-described trajectory registration process. These parameters are given in Table I. The physical pixel size on the flat panel detector is 0.154 mm; a 2-by-2 binning mode was considered. Also, the detector was used in the landscape mode.

Distance from source to isocenter (R)	786 mm
Distance from source to detector (D)	1198 mm
Radius of the FOV (r)	125 mm
Scanning range	198^o
Number of Projections	496
Detector pixel size	0.308 mm
Detector size	1240x960

TABLE I: Parameters for the ideal geometry

Real data of the anthropomorphic head phantom were obtained on the same research-dedicated Siemens Artis C-arm system. We considered data acquisition with normal head positioning as well as data acquisition with the head tilted by 20 degrees, as shown in Figure 3. In clinical practice, the C-arm rotation would be tilted not the phantom. For this early evaluation, tilting the phantom was easier to implement.

All data sets were reconstructed using the ACE method [2]. This method was primarily preferred over the approach in [1] to make the test more challenging, as the smooth weights in [1] could have easily masked undesirable effects of the interpolation. An isotropic voxel size of 0.49 mm was used.

B. Results with the FORBILD head phantom

Figure 4 shows the reconstruction in the plane of the circular scan under three different settings: (i) ideal data, (ii) rebinned data, and (iii) brute-force reconstruction of non-ideal data without rebinning (wrongly assuming the data is in the ideal geometry). The difference between (ii) and (i), and also

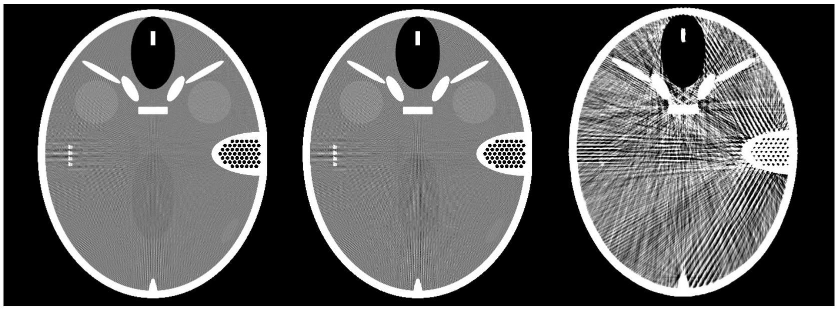

Fig. 4: Reconstruction using the ACE method, shown in the (x, y)-plane. From left to right: reconstruction using projection from the ideal trajectory, using rebinned projection data, and directly using the non-ideal projection data by wrongly assuming that they are in the ideal geometry. Grayscale: $[-50, 150]$ HU.

between (iii) and (i) is shown in Figure 5. Figures 6 and 7 show the same arrangement of results for reconstruction in the (y, z)-plane. These results show that the non-ideal data differs too much from the ideal geometry to provide accurate reconstructions without considering the geometry deviations. The suggested rebinning algorithm allows accounting for these deviations; the results show that it provides attractive results with no apparent resolution loss.

To further assess the quality of the suggested rebinning algorithm, we performed zoomed reconstruction on the resolution pattern in the (x, y)-plane of the phantom. See Figures 8, 9, and 10. Moreover, we also assessed the MTF in the (x, y) plane and the slice sensitivity profile (SSP) along the z-axis, from reconstructions of a cylindrical object centered on the origin and parallel to the z-axis (diameter of 4 cm and height of 8 cm). The MTF and the SSP are shown in Figures 11 and 12 respectively. These five figures show that there is no loss of resolution in (x, y) and also no loss of resolution in z. Importantly, note also that the MTF for the rebinned data reaches its first zero at the same location as the MTF for the ideal data. Thus, resolution can be adapted in the same way for both ideal and rebinned data.

C. Head Scan

Results obtained from the real data of the anthropomorphic phantom are shown in Figures 13 and 14. The first figure compares reconstruction using SS-FDK to reconstruction using the ACE method, both from rebinned data. A fair mitigation of CB artifacts can be observed, supporting clinical value for advanced image reconstruction methods that handle redundancies in the data set in a rigorous way (not like the SS-FDK method). The suggested rebinning algorithm allows utilizing such advanced methods directly, i.e., in their original formulation for ideal trajectories. The second figure compares data acquisition without and with a simulated geometry tilt. It can be seen in this figure that there can be benefits in terms of CB artifacts to using a geometry tilt as in diagnostic CT. The benefits may however be dependent on positioning of the region-of-interest: tilting the geometry does not avoid CB artifacts; it displaces them to locations that may be more advantageous for some clinical applications.

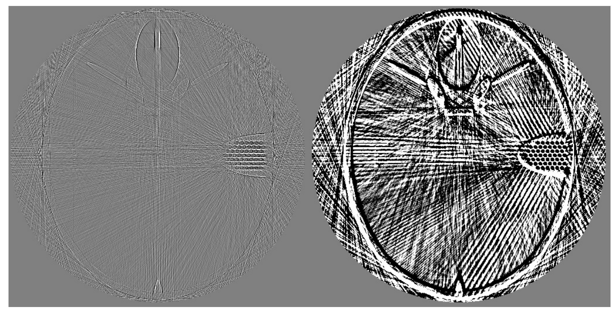

Fig. 5: Differences between reconstruction results in the (x, y)-plane. Left: for ideal minus rebinned projection data. Right: for ideal minus non-ideal projection data. Grayscale: $[-20, 20]$ HU.

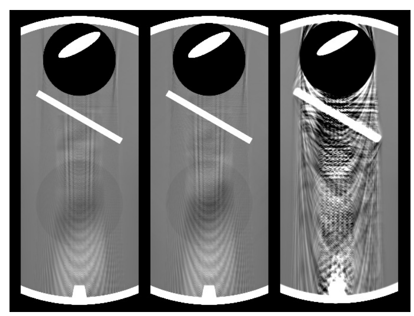

Fig. 6: Reconstruction using the ACE method, shown in the (y, z)-plane. From left to right: reconstruction using projection from the ideal trajectory, using rebinned projection data, and directly using the non-ideal projection data by wrongly assuming that they are in the ideal geometry. Grayscale: $[-50, 150]$ HU.

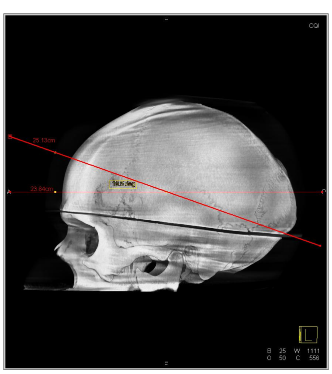

Fig. 3: Setup for real data acquisition of an anthropomorphic head phantom that is tilted to simulate a data acquisition with a gantry tilt, as used in diagnostic CT imaging. The oblique and horizontal red lines show the classical and tilted trajectory planes selected for our experiment.

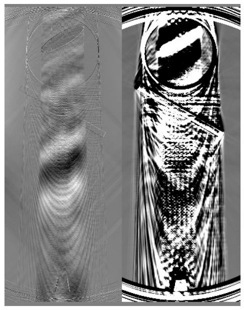

Fig. 7: Differences between reconstruction results in the (y, z)-plane. Left: for ideal minus rebinned projection data. Right: for ideal minus non-ideal projection data. Grayscale: $[-20, 20]$ HU.

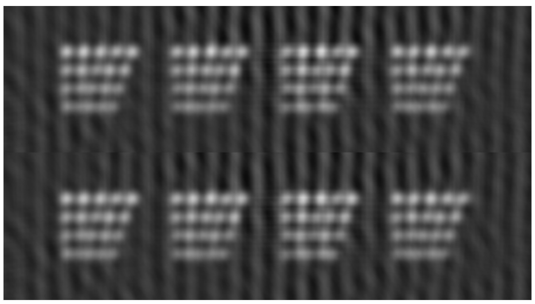

Fig. 8: Reconstruction using the ACE method zoomed on the resolution pattern in the (x, y)-plane. Top: ideal data. Bottom: rebinned data. Grayscale: $[-50, 450]$ HU.

V. Conclusion

We have suggested a rebinning algorithm that allows transforming data from a floor or ceiling mounted C-arm system, or from a robotic system, into data acquired in an ideal geometry. This rebinning algorithm enables utilization of advanced CB reconstruction methods to mitigate CB artifacts. We extensively evaluated the performance of the algorithm using the FORBILD head phantom as well as a cylindrical phantom to assess MTF and SSP. The results show the performance of the rebinning algorithm is very good. Furthermore, we have applied the rebinning algorithm to real data of an anthropomorphic phantom. This additional experiment demonstrated clinical value of our rebinning algorithm, particularly as a fair mitigation of CB artifacts can be seen in comparison with the SS-FDK algorithm. Last, we showed that data acquisition with the equivalent of a gantry tilt can provide, in terms of CB artifacts, additional improvements within some regions of the brain.

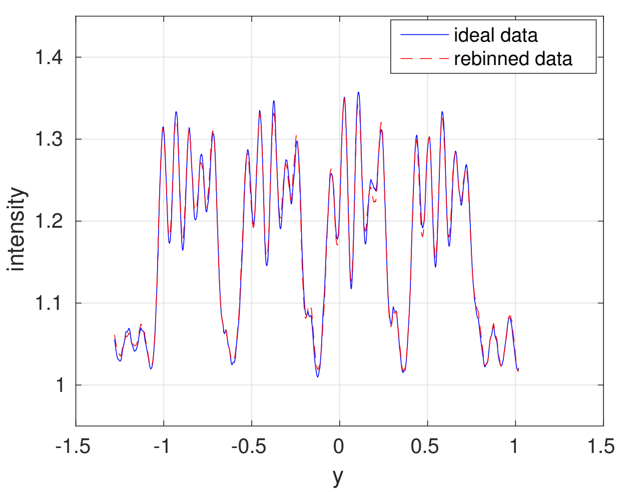

Fig. 9: Profile through the top row of ellipsoids in the resolution pattern (as displayed in Figure 8). The solid line corresponds to the ideal data, and the dashed line to the rebinned data.

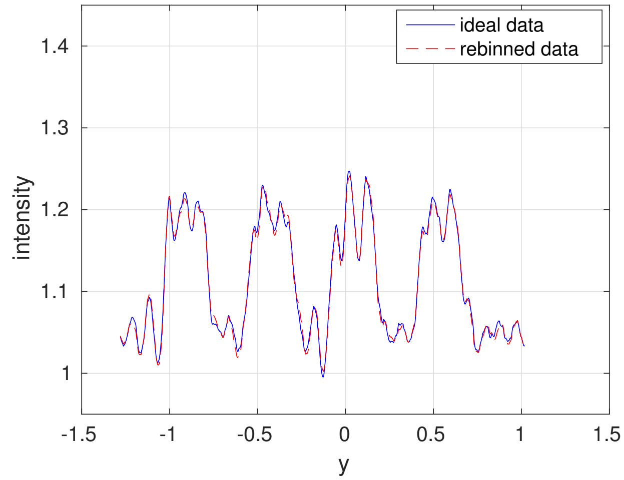

Fig. 10: Profile through the bottom row of ellipsoids in the resolution pattern (as displayed in Figure 8). The solid line corresponds to the ideal data, and the dashed line to the rebinned data.

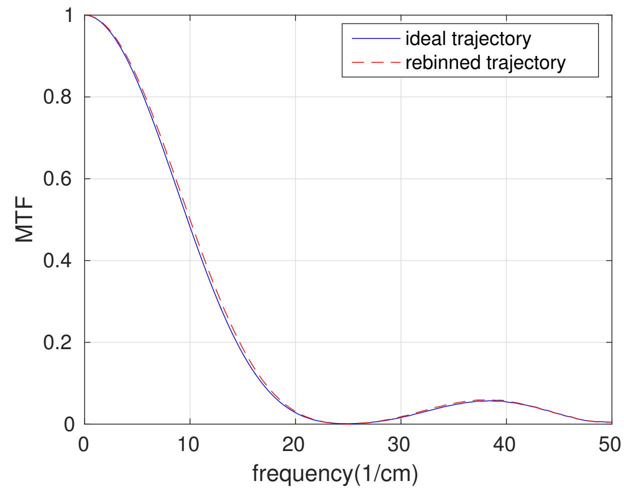

Fig. 11: Modulation transfer function in the (x, y)-plane. The solid line represents the MTF of ideal trajectory, and the dashed line shows the MTF of the rebinned trajectory.

Disclaimer

The concepts and information presented in this paper are based on research and are not commercially available.

Acknowledgment

This work was partly supported by the Erlangen Graduate School in Advanced Optical Technologies (SAOT); the authors

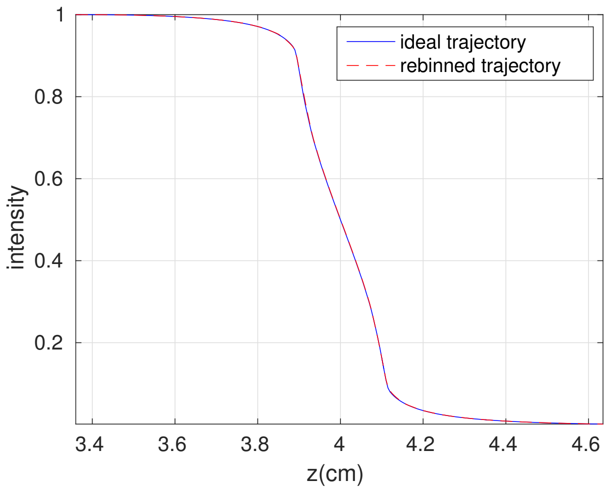

Fig. 12: Slice sensitivity profile (SSP) along the z-axis. The solid line is the SSP for the ideal trajectory, and the dashed line is the SSP for the rebinned data. The vertical axis is the recontructed linear attenuation coefficient normalized to unity for water.

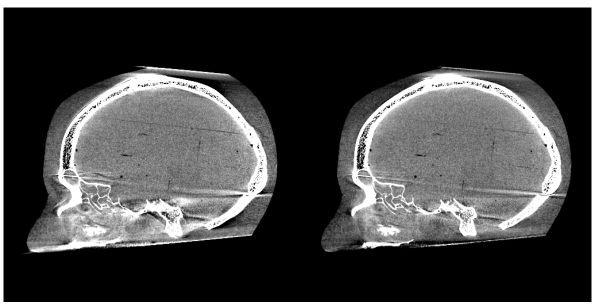

Fig. 13: Reconstruction from real data of an anthropomorphic head phantom. Left: using SS-FDK. Right: using the ACE method. Grayscale: $[0.2, 0.32]$/cm.

gratefully acknowledge funding of SAOT by the German Research Foundation (DFG) in the framework of the German excellence initiative. This work was also supported by a research contract with Siemens Healthcare, GmbH.

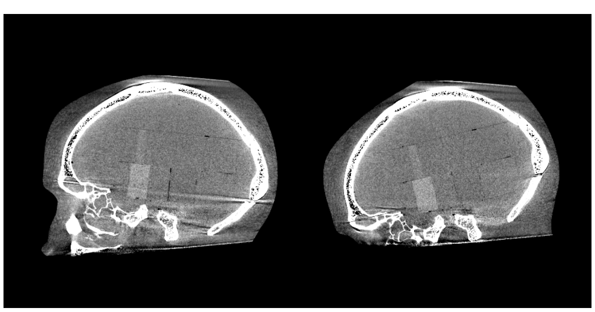

Fig. 14: Reconstruction from real data of an anthropomorphic head phantom using the ACE method with our rebinning algorithm. Left: conventional positioning of the head. Right: tilted positioning of the head, simulating a CT-like gantry tilt with the C-arm system. Grayscale: $[0.2, 0.32]$/cm.

REFERENCES

[1] Noo, F. and Heuscher, D. J., "Image reconstruction from cone-beam data on a circular short-scan," in [*Medical Imaging 2002*], 50–59, International Society for Optics and Photonics (2002).

[2] Nett, B. E., Zhuang, T.-L., Leng, S., and Chen, G.-H., "Arc based cone-beam reconstruction algorithm using an equal weighting scheme," *Journal of X-Ray Science and Technology* **15**(1), 19–48 (2007).

[3] Dennerlein, F., Noo, F., Schondube, H., Lauritsch, G., and Hornegger, J., "A factorization approach for cone-beam reconstruction on a circular short-scan," *IEEE transactions on medical imaging* **27**(7), 887–896 (2008).

[4] Yu, L., Zou, Y., Sidky, E. Y., Pelizzari, C. A., Munro, P., and Pan, X., "Region of interest reconstruction from truncated data in circular cone-beam ct," *IEEE transactions on medical imaging* **25**(7), 869–881 (2006).

[5] Hoppe, S., Hornegger, J., Dennerlein, F., Lauritsch, G., and Noo, F., "Accurate image reconstruction using real c-arm data from a circle-plus-arc trajectory," *International journal of computer assisted radiology and surgery* **7**(1), 73–86 (2012).